Measurement of G-phase volume fraction and number density in duplex stainless steels using transmission electron microscopy

Isak McGieson,[1] Jonathan D. Poplawsky,[2] Melissa K. Santala,[3,4a] and Julie D. Tucker,[3,4]

[1] *Department of Physics, Oregon State University, Corvallis, OR, USA*
[2] *Center for Nanophase Materials Sciences, Oak Ridge National Laboratory, Oak Ridge, TN, USA*
[3] *Materials Science Program, Oregon State University, Corvallis, OR, USA*
[4] *School of Mechanical, Industrial, and Manufacturing Engineering, Oregon State University, Corvallis, OR, USA*

ABSTRACT

Duplex stainless steels (DSS) have a high toughness and strength due the presence of both austenitic and ferritic phases. These alloys have had limited use in power production applications due to thermal embrittlement caused by spinodal decomposition and development of G-phase precipitates in the ferrite. Lean grade DSS alloys (e.g., 2101, 2003) may offer improved thermal stability due to the reduction of Cr- and Ni-equivalent elements when compared to standard grade compositions (e.g., 2205, 2209). The abundance of the G-phase was measured in five duplex stainless steels, three wrought alloys (2101, 2003, 2205) and their matching filler metals (2101-w, 2209-w), after aging at 427°C for 1,000 h and 10,000 h. The G-phase volume fraction, number density, size, and precipitate spacing were found using quantitative analysis of transmission electron microscopy dark field images and the composition of G-phase precipitates on other clusters were characterized with atom probe tomography (APT). In the welded alloys, the G-phase was found to develop rapidly, relative to the wrought material. A positive correlation was found between the nickel equivalent composition of the alloy and the G-phase volume fraction. The alloys 2205, 2209, and 2101-w, which are higher in Cr and Ni, all showed significant G-phase precipitation, further strengthening the hypothesis that lean grade DSS alloys are more thermally stable against precipitation in the ferrite. Electron diffraction showed a secondary phase present in the 2101 wrought alloy at 10,000 h, but it was not crystallographically consistent with the G-phase; APT showed the presence of nanoclusters rich in both nickel and copper for this alloy. No secondary phases or clusters were found in 2003 after 10,000 h of aging, so it may be a candidate alloy for applications that require long-life times at high operating temperatures.

Keywords: duplex stainless steel (DSS); G-phase; transmission electron microscopy (TEM); atom probe tomography (APT)

[a] Corresponding author, e-mail: melissa.santala@oregonstate.edu

1. INTRODUCTION

Duplex stainless steels (DSS) have high toughness, strength, and excellent corrosion resistance with a relatively low nickel content. This combination of properties results from a roughly equal ferrite and austenite phase fraction and makes DSS a choice material for piping, pressure vessels, storage tanks, and structural components in chemical processing industries [1]. Despite the advantages of DSS, use in industrial applications (i.e., power production) has been limited due to thermal embrittlement during long term operation at temperatures between 200°C and 580°C [2].

Thermal embrittlement is caused by a phase separation in the ferrite into a chromium-rich α′ phase from the iron-rich α phase through either spinodal decomposition or nucleation and growth [2]. Following α-α′ phase separation, a face-centered cubic precipitate called the G-phase can form [3, 4] from the nickel, manganese, and silicon [5] rejected during phase separation, often at the α-α′ interfaces. Both G-phase formation and α-α′ phase separation may contribute to the degradation of mechanical properties during aging, though their relative contributions to thermal embrittlement varies depending on the alloy composition and thermal history [6-12]. Badyka *et al.* [10] quantified spinodal wavelength and amplitude and G-phase particle size in eight aged Mo-free and Mo bearing DSS (including 2101 and 2205) and used combinations the Ardell model and either the modified Orowan or a modified Bacon-Kocks-Scattergood model to estimate the relative influence of spinodal decomposition and G-phase on hardening. They showed that G-phase contributes to hardening and is the main contributor to the hardening of the Mo-bearing steels they studied in the early stages of aging in the range of 323°C to 350°C. Silva *et al*. [11] compared hardness of 2205 and 2101 DSS that had been aged at 475°C with aged alloys that were annealed to reverse spinodal decomposition without dissolving precipitate phases. They attributed only 2% of hardening to G-phase precursors and other precipitates contribute in 2101, but 17% of hardening

in 2205 was attributed to the G-phase. The same study also demonstrated that the G-phase and other precipitate phases contribute to a decrease in pitting corrosion resistance, however Cr-depletion due to spinodal decomposition was the dominant contributor in 2205. In 2101, Cr-rich nitride precipitates impacted corrosion resistance more that spinodal decomposition. G-phase has also been found to dominate the decrease in pitting corrosion resistance in aged DSS Fe20Cr9Ni [13]. Thus, even if the G-phase does not dominate hardness increases during aging, it may degrade corrosion resistance.

The kinetics of α-α′ phase separation and subsequent G-phase precipitation are affected by the alloy composition, so identification of alloys with slower aging kinetics could make DSS an appropriate choice for applications that require long term operation at elevated temperatures. Lean grade alloys, such as 2003 and 2101, have relatively low chromium- and nickel-equivalent elements (which include copper, nitrogen, and carbon) [14], and are a grade of DSS alloys that show promise for these applications. In this study, G-phase formation in lean grade alloys 2101 and 2003 and their matching weld metal (2101-w) are compared to the most common standard grade DSS 2205 and its matching weld metal (2209-w). Understanding the characteristics and composition dependence of G-phase formation might assist in the selection of suitable alloys for elevated temperature applications.

The G-phase has been identified previously using transmission electron microscopy (TEM) and atom probe tomography (APT) over a range of temperatures (300°C to 470°C) and aging times (0 h to 20,000 h). The crystallographic relationship between the G-phase and the ferrite matrix has been determined to be $(100)_{\alpha}||(100)_{G}$; $[010]_{\alpha}||[010]_{G}$, or "cube-on-cube" orientation using electron diffraction [5, 15-19]. High resolution TEM has been used to verify this orientation and measure the lattice mismatch between the G-phase and ferrite matrix [17, 19]. That the precipitates

identified in the APT experiments are crystallographically distinct from the ferrite matrix has been verified with dark field TEM (DF-TEM) [15, 16, 18]. Quantitative measurements of the G-phase volume fraction in the aged alloys have been made using APT [16, 17, 19] and number density and precipitate size have been measured using both APT and TEM [10, 15, 16, 18]. The chemistry of the G-phase has been measured using TEM energy dispersive spectroscopy (EDS) [17, 19] and APT [16-18].

In this work, G-phase is investigated in five candidate DSS alloys aged for up to 10,000 h. DF-TEM and energy filtered TEM (EF-TEM) based thickness maps were used to quantify the abundance of the G-phase. Specifically, the volume fraction, number density, precipitate size and precipitate separation were calculated. In previous work with the same alloys, the evolution of α-α′ phase separation [3, 20, 21], change in the hardness of the ferrite [2, 3, 21], and the corrosion resistance [22] were measured. The leaner grade alloys were found to have a slower hardening rate, but reduced corrosion resistance. The characterization of the G-phase in this set of alloys completes the comparison of lean versus standard grade DSS alloys after thermal aging at 427°C.

2. Materials and Methods

Five DSS alloys were studied: three commercial, hot-rolled wrought alloys, 2101, 2003, and 2205, and two welded alloys, 2101-w and 2209-w. The weld deposits were made through a multi-pass gas tungsten arc welding process in which large weld pads (approximately 13 cm × 11 cm × 16 cm) were created using 2101-w and 2209-w weld wire. The welds were made on their corresponding base metals, 2003 and 2205, respectively. The microstructural characterization of the as-received alloys has been described elsewhere [4, 21]. The weld pads were cut from the base metal and sectioned into bars for isothermal aging. Bars of all five alloys were aged isothermally at a temperature of 427°C for up to 10,000 h, air cooled, and then machined into test samples. Two

of these alloys, 2101 and 2003 are considered lean grade alloys, while 2205 and 2209-w, are considered standard grade alloys. The 2101-w matching weld metal is recommended for welding wrought 2101 and 2003 but is over-alloyed to compensate for chemical segregation that occurs during welding. The 2101-w composition is within the standard grade composition range. The chemical compositions of all five alloys are shown in Table 1. The compositions of alloys 2101 and 2205 were provided by the alloy vendor's certified material chemistries. Alloy 2003 chemistry was determined by an independent testing company using methods specified in ASTM A 751-08 and ASTM E 1019-0. Two samples from each weld build-up of alloys 2101-w and 2209-w were tested by an independent testing company using inductively coupled plasma atomic emission spectroscopy and methods in ASTM E 1018-08. The chemistries from the two samples of each alloy were averaged and reported in Table 1.

Table 1: Chemical composition of the five alloys studied (wt. %).

Alloy	**Fe**	**Cr**	**Ni**	**Mo**	**Mn**	**Si**	**N**	**C**	**Cu**
2101	Bal.	21.49	1.54	0.21	5.00	0.79	0.21	0.029	0.30
2003	Bal.	21.22	4.48	1.63	1.20	0.39	0.18	0.03	0.13
2205	Bal.	22.44	5.69	3.11	1.80	0.42	0.17	0.020	0.43
2101-w	Bal.	23.30	7.34	0.24	0.78	0.46	0.18	0.02	0.14
2209-w	Bal.	22.49	8.59	3.05	1.50	0.48	0.18	0.02	0.15

The ferrite region of each aged alloy was characterized with APT. Sample preparation, data collection methods and the evolution of α-α′ phase separation are reported elsewhere [2, 3, 20-22]. In this paper, we reanalyzed the data to obtain chemical information for the G-phase and other precipitates. Proximity histograms were generated for each alloy using a 15 at.% Ni isoconcentration surface to identify the surface of the precipitate. The surface was formed using a 0.5 × 0.5 × 0.5 nm grid and 3 × 3 × 3 nm delocalization. The mass spectrum ranging was kept the same for each sample.

Slices for TEM sample preparation were cut from the aged DSS bars using a Buelher IsoMet 1000 low speed saw. The samples were thinned to approximately 100 μm thick foils and one side was polished to a 1 μm finish with an alumina suspension. Three-millimeter diameter discs were punched from the foils and a Gatan 657 Dimple Grinder II was used to dimple the discs, leaving approximately 15 μm at the thinnest point. The dimpled samples were ion milled to perforation using a Gatan PIPS II argon ion mill operated at 7 keV.

Bright field images, dark field images, selected area electron diffraction (SAED) patterns and thickness maps were collected from ferrite grains using an FEI Titan operated at 200 keV. The G-phase was identified in the SAED pattern as a secondary fcc phase with a cube-on-cube orientation relationship with the bcc ferrite and a lattice parameter roughly four times that of the ferrite [17]. Energy filtered TEM (EFTEM) images were taken using a Gatan Imaging Filter Tridiem and thickness maps were calculated from the total intensity image, elastic scattering image, and the mean free path. The mean free path used in the calculation was the average of the electron mean free path of each element [23] in the composition [4] of the ferrite, weighted by its atomic percent.

An image processing pipeline was developed to extract quantitative measurements of the apparent area fraction of the G-phase from the dark field images based on the image intensity. The dark field images were first segmented into three phases: vacuum, ferrite, and G-phase. To prepare images for segmentation, manually drawn masks were used to remove complicating features, such as bend contours and grain boundaries. Simple histogram-based segmentation is insufficient due to the non-uniform intensity of the G-phase and other phases caused by heterogeneities in specimen thickness, local orientation, and chemical composition [16]. Instead, the random walker segmentation algorithm [24] was chosen to label pixels into the

three phases. This algorithm requires user provided seed points for each phase. These were selected by a manual threshold for the vacuum and the G-phase. The ferrite phase seed points were what remained, with an unlabeled buffer region between all phases. The random walker algorithm uses the seed points to label the pixels in the buffer region by solving an anisotropic diffusion problem with sources at the seed points and the local diffusion constant increasing with the similarity of adjacent pixels [24]. The segmentation resulted in small artifacts, so a minimum cutoff size had to be chosen. Since 1.3 nm has been measured to be the critical radius for the transformation of nascent G-phase solute clusters to crystallographically distinct precipitates [18], it was chosen as the cutoff radius.

Thickness maps corresponding to the dark field images of the G-phase were extracted from lower magnification thickness maps with a two-step image registration process. First, the higher magnification dark field image was registered to a lower magnification overview dark field image. Then, the lower magnification dark field was registered to the EFTEM thickness map. This enabled a thickness map of the higher magnification dark field image to be extracted from the lower magnification thickness map, avoiding the need to aligning two detectors to precisely the same sample region.

The quantitative results were calculated based on the segmented higher magnification dark field and the corresponding thickness map. For each precipitate in each segmented image, the radius, r, the roundness, R (used to calculate the error in r), and the centroid were calculated. Each r was determined by the equal area circle for each precipitate, and R by equation (1) with precipitate area A, and perimeter P. For a circle, the roundness is 1. The uncertainty in r, δr, was calculated using equation (2). A spherical grain approximation with r as the radius was used to estimate the volume of each precipitate, and δr, the error in the volume.

$$R = 4PA/P^2 \quad (1)$$

$$\delta r/r = 1 - R \quad (2)$$

The total G-phase volume, V_G, was calculated by summing the spherical volumes. Integration of the thickness map subframe, ignoring any manually masked regions, yielded the total volume, V, from which the G-phase volume fraction, V_G/V, was calculated. The centroids of each segmented precipitate were used to calculate the nearest neighbor distribution, its median being the reported precipitate spacing, d. The precipitate number density, n, was calculated using V and the number of observed precipitates.

3. RESULTS AND DISCUSSION

Crystallographically distinct G-phase precipitates larger than the critical radius of 1.3 nm were observed in dark field images in the 10,000 h samples of 2205, 2101-w and 2209-w, and the 1,000 h samples of 2101-w and 2209-w. Visible G-phase precipitates were absent in 2003, 2101 at both 1,000 h and 10,000 h, and the 1,000 h sample of 2205. Alloys 2003 and 2101 have the lowest nickel content of the five alloys chosen for this study and are the only two with no G-phase present after aging for 10,000 h. Although 2101-w is the matching weld alloy for the Ni-lean 2101, it is "over-alloyed" with nickel (see Table 1) to compensate for chemical segregation during welding. For 2101, a secondary phase was present in the diffraction pattern at 10,000 h. The lattice parameter and orientation relationship are inconsistent with the G-phase. This secondary phase may be the nascent solute clusters only partially transformed into the G-phase as discussed with the APT results. In 2003, no secondary phase was identified after aging for 10,000 h. For the samples without visible G-phase precipitates there were no dark field images to analyze, so the G-phase volume fraction was approximated as zero. Table 2 shows the measured lattice parameters (a_F for ferrite, and a_G for the G-phase) for the samples

in which the G-phase could be unambiguously identified by its crystallographic features in SAED patterns.

Table 2: Lattice parameter measurements based in electron diffraction pattern analysis for samples that unambiguously contained the G-phase. The lattice parameters a_F and a_G are for ferrite and the G-phase, respectively, and have an estimated error of ±0.01 nm. The expected a_G/a_F ratio is four [4].

Aged (h)	Alloy	a_F (nm)	a_G (nm)	a_G/a_F
10000	2205	0.29	1.18	4.1
10000	2101-w	0.29	1.14	3.9
10000	2209-w	0.30	1.28	4.3
1000	2101-w	0.29	1.25	4.3
1000	2209-w	0.29	1.26	4.3

Figure 1 shows a bright field/dark field image pair of 2101-w aged for 10,000 h with distinct cubic G-phase precipitates.

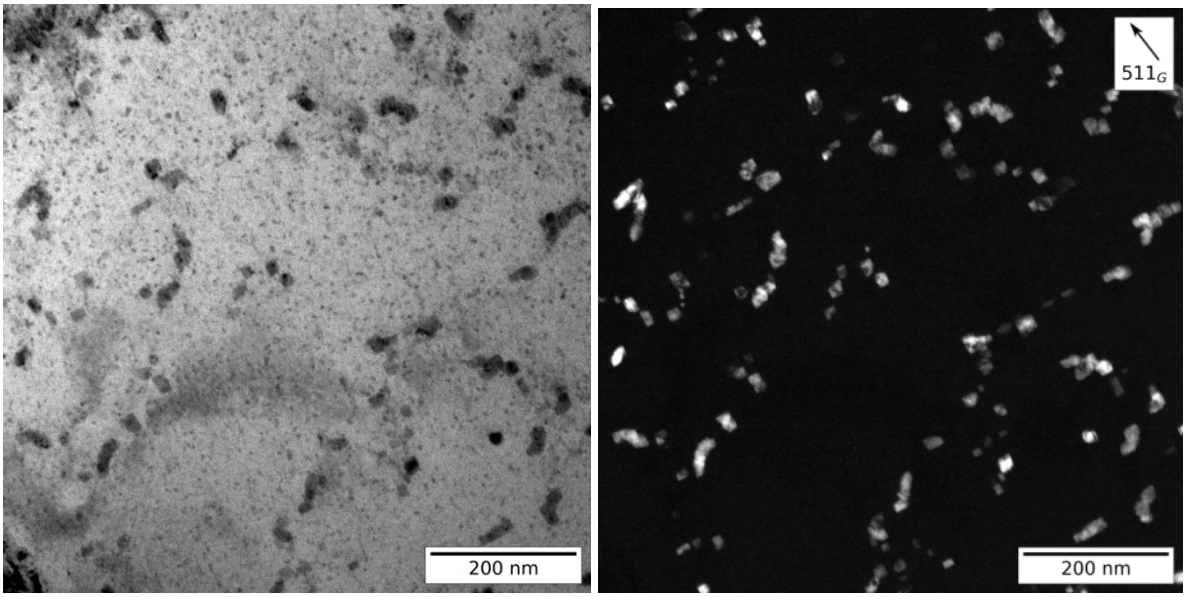

Figure 1: Bright field (left) and dark field (right) image pair of 2101-w aged for 10,000 h. The G-phase precipitates are darker than the ferrite matrix in the bright field due to the higher local concentration of nickel. The G-phase appears bright in the dark field because a G-phase reflection was used to form the image. Figure S1 of the Supplementary Material shows the SAED pattern associated with the dark field image.

The low magnification dark field image in Figure 2 gives a broader overview of the distribution and morphology of the G-phase in 2101-w specimens aged for 1,000 h and 10,000

h. The development of the G-phase in 2101-w between 1,000 h and 10,000 h is apparent by comparison of images in Figure 2.

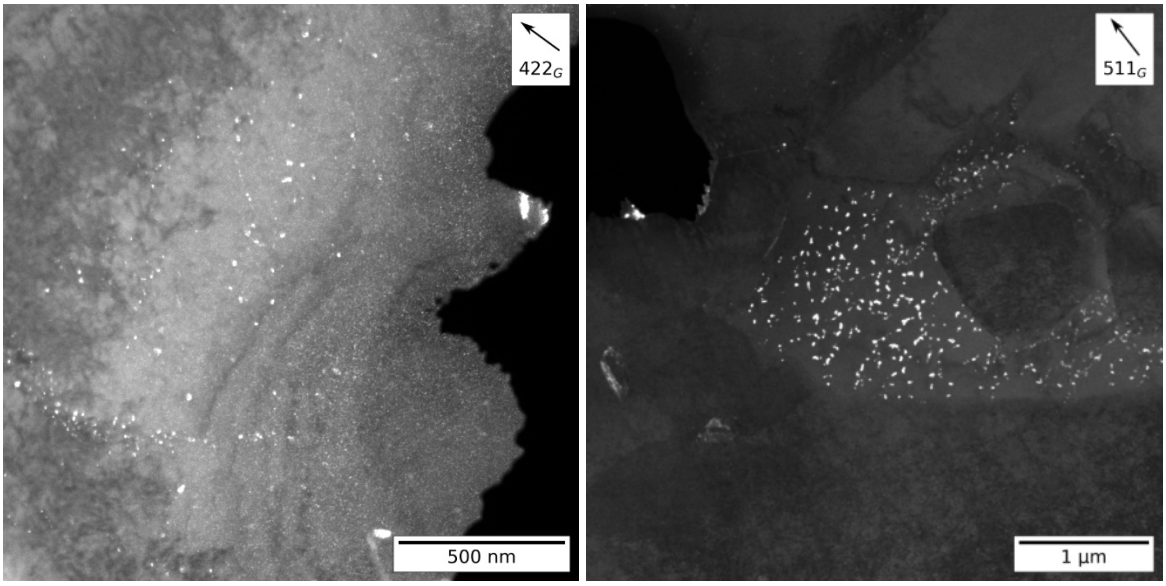

Figure 2: A low magnification dark field of 2101-w aged for 1,000 h (left) and 10,000 h (right). The 10,000 h dark field shows both austenite and ferrite grains. The austenite grains do not contain the G-phase. Figures S2 and S1 in the Supplementary Material show the associated SAED patterns.

Dark field images for 2209-w aged for 1,000 h and 10,000 h are shown in Figure 3. A lower magnification dark field for the 10,000 h sample giving a broader overview of the distribution of the G-phase is shown in Figure 4. For this alloy, the G-phase forms chains of precipitates and decorates the grain boundaries, a growth characteristic not observed in the other alloys. The 2101-w G-phase also forms in chains, though less so than 2209-w.

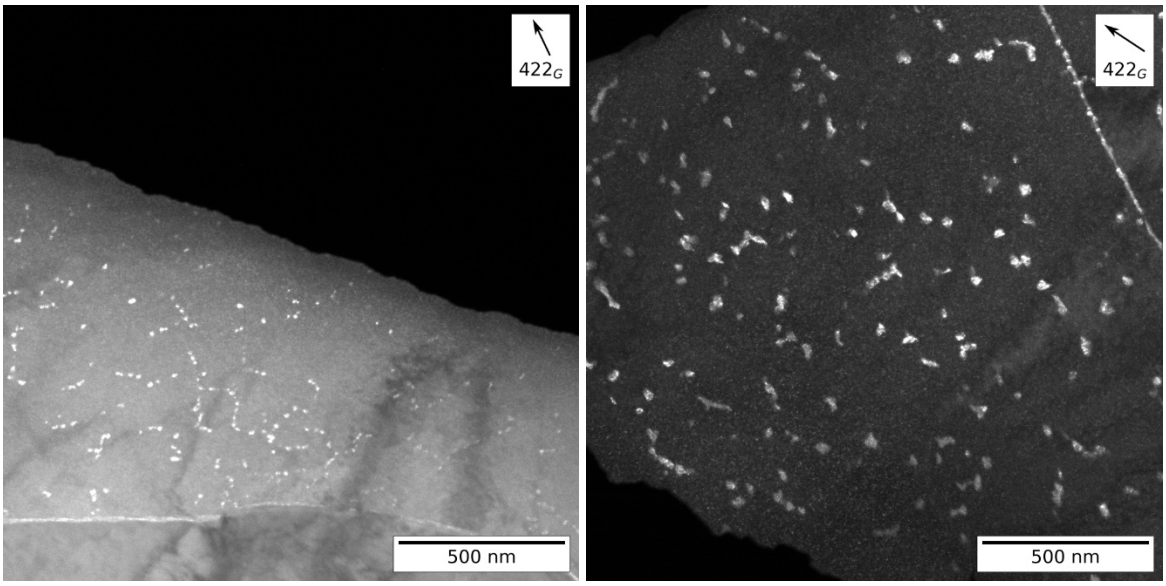

Figure 3: Dark field images from 2209-w aged for 1,000 h (left) and 10,000 h (right) shown at the same scale highlighting the coarsening of the G-phase. Figures S3 in the Supplementary Material show the associated SAED.

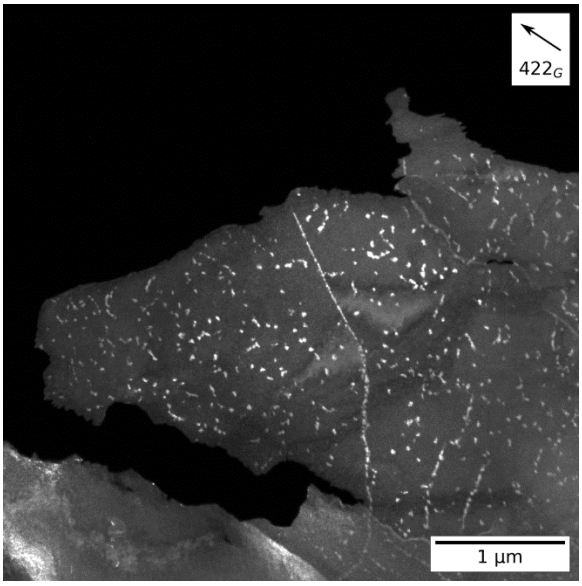

Figure 4: A low magnification dark field of 2209-w aged for 10,000 h. The G-phase is more developed and forms longer chains at this aging time as compared to 1,000 h sample in Figure 3 (left). Figure S4 in the Supplementary Material shows the associated SAED.

In 2205, the G-phase is more uniformly distributed than the other alloys, as seen in Figure 5. The thermal history and heterogeneities introduced by multi-pass welding likely contribute to this difference in morphology of the G-phase between the welded samples and wrought samples.

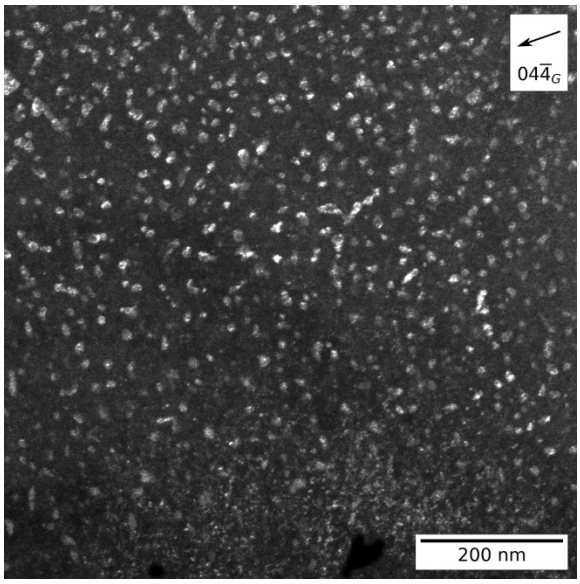

Figure 5: A dark field image from 2205 aged for 10,000 h shows the G-phase distribution. Figure S5 in the Supplementary Material shows the associated SAED.

From the dark field segmentation, the distribution of nearest neighbor distances and grain roundness were calculated. Histograms of these quantities are shown in Figure 6. The relatively uniform distribution of the G-phase in 2205 that is visually apparent in Figure 5 yields the narrow distribution of nearest-neighbor distances in the histogram in Figure 6 (left). G-phase coarsening is captured by the increase in median nearest-neighbor distance, d, with aging time, reported quantitatively in Table 3, and in the histogram in Figure 6 (left).

The individual G-phase precipitates are relatively equiaxed in all specimens, with most precipitates having a roundness >0.5 (or equivalently an aspect ratio <2), though they are aligned in chains for some specimens, which suggests they are developing along planar defect or dislocations in the ferrite, as observed by others [6, 25]. The histograms show an apparent decrease in median roundness in both 2101-w and 2209-w between 1000 and 10,000 h of aging, however the decrease in 2101-w is within the error of the measurements. Other researchers have found a decrease in roundness with aging due to an increase in lattice mis-fit between the G-phase and

ferrite with aging in DSS Fe20Cr9Ni [13, 19], which they attribute to a reduction in the strain energy caused by the formation of plate-like morphology. Based on the ratios of lattice parameters for 2101-w, which comes closer to an integer value of 4 between 1,000 and 10,000 h, an increase in roundness might be expected, due to a decrease in misfit between the G-phase and the ferrite. An increase in roundness would reduce the excess interfacial free energy. There is no change in the G-phase:ferrite lattice parameter ratio for 2209-w between 1,000 and 10,000 h, but the reduction in roundness with aging is more significant in 2209-w than 2101-w. Since the 1,000 h and 10,000 h images are from different specimens, the change in roundness may be due to microstructural variations within the specimen rather than a systematic change in particle morphology with aging. However, the decrease in roundness may also be due the development and coarsening of the G-phase on dislocations, in which case both effect of enhanced pipe diffusion and energetic advantage of growing the precipitate along the defect would contribute to enhanced growth in parallel to the direction of the line defect.

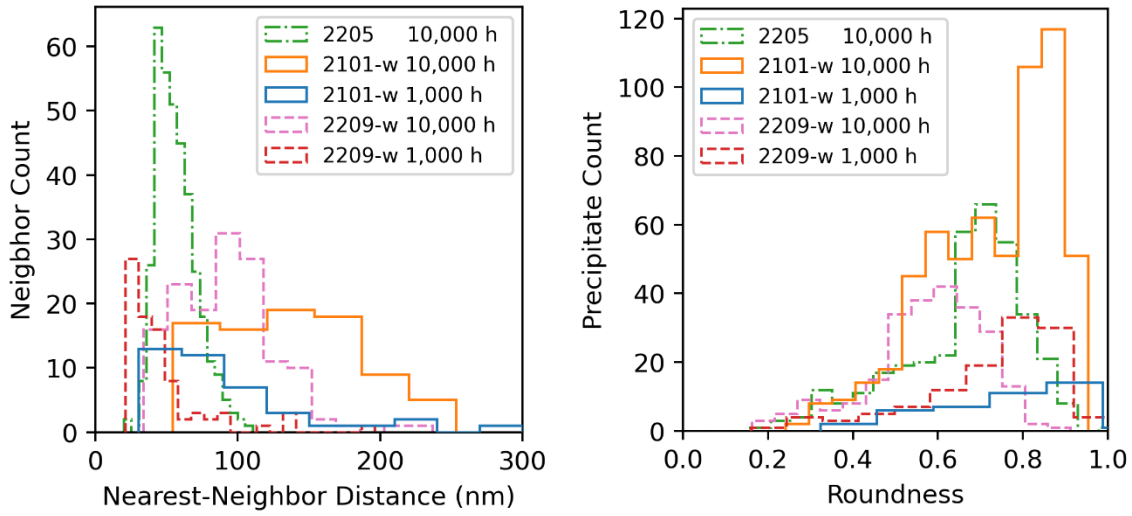

Figure 6: Histograms of nearest-neighbor distances (left) and grain roundness (right), calculated using quantitative image analysis as described in the methods section. The shift to greater spacing from 1,000 h to 10,000 h for 2101-w and 2209-w samples is due to coarsening. There is a slight reduction in median roundness with aging in 2209-w.

Table 3 shows the total sample volume, V, and the G-phase volume fraction, V_G/V, calculated from thickness maps and segmented dark field images. The intensity at any point of a dark field image comes from the intensity of the diffracted beam used to form the image (as indicated by the indexed arrow in each dark field image). Any G-phase precipitate that is not oriented to diffract the select beam, will not have a high intensity in the image. This means the reported volume fraction and number density measurements are lower bounds. For the 10,000 h samples, all precipitates are expected to be identified, but for the 1,000 h samples some precipitates may have been missed [16].

Previously reported APT measurements of the volume fraction for identical samples [4] were a few percent lower than the values reported here, which may be a consequence of the smaller sample volumes observed. The uncertainty in the volume fraction decreases with rounder precipitates, and it may be seen in reference to Figure 6 (left) and Table 3, that the uncertainty for the 2101-w sample aged for 1,000 h, for example, is less than that for the 2209-w sample aged for 1,000 h, consistent with the roundness distribution for 2101-w being closer to one than 2209-w.

Table 3: Quantitative image analysis results for samples with unambiguous G-phase precipitates. d is the median precipitate spacing, n the total precipitate number density, r the median precipitate radius, V the observed volume, and V_G the observed G-phase volume. The uncertainty in r and d are the standard error of the median, in n, the square root of the number of precipitates, and, in V, the propagated error from the spherical grain approximation.

Aged (h)	Alloy	d (nm)	n (1/m^3)	r (nm)	V (m^3)	V_G (m^3)	V_G/V
10000	2205	55(1)	$1.85(9) \times 10^{22}$	7.0(2)	2×10^{-20}	9×10^{-22}	0.046(6)
10000	2101-w	112(4)	$1.13(4) \times 10^{21}$	11.9(3)	5×10^{-19}	8×10^{-21}	0.015(2)
10000	2209-w	99(6)	$1.40(9) \times 10^{21}$	17.1(6)	2×10^{-19}	9×10^{-21}	0.05(1)
1000	2101-w	75(16)	$7(1) \times 10^{20}$	7.2(5)	6×10^{-20}	1×10^{-22}	0.0017(3)
1000	2209-w	40(9)	$1.8(1) \times 10^{21}$	7.2(3)	6×10^{-20}	3×10^{-22}	0.005(2)

The histogram of precipitate number density for a given precipitate radius is shown in Figure 7, and the total number density, n, along with the median precipitate radius, r, is shown

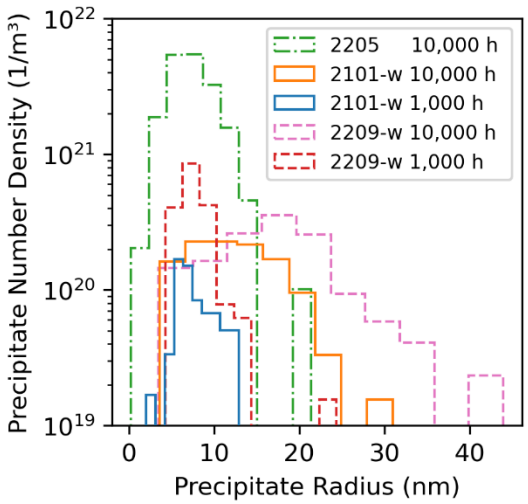

Figure 7: A histogram of number density for a given precipitate radius, calculated using quantitative image analysis as described in the methods section.

in Table 3. Another effect of coarsening is captured by the increase in *r* between 1,000 h and 10,000 h of aging time. Previous work on identical samples [4] measured the G-phase precipitate number density using APT and found it to be consistently higher than that reported here by one to two orders of magnitude. This could be caused by the identification in the APT analysis of solute clusters as G-phase based on chemistry rather than diffraction, which would be missed from the precipitate count by the methods used here. It has long been recognized that SAED based detection of G-phase may not detect the smallest precipitates, and thus will underestimate volume fraction and overestimate average size [25]. In the same work [4], at 10,000 h, the 2101 sample was found to have an order of magnitude lower precipitate density than the 2205 sample aged for 10,000 h. This is qualitatively consistent with the finding here that the secondary phase is much less developed in 2101 than in 2205.

APT results were analyzed for the alloys showing some form of precipitates to characterize the precipitate chemistry. Proximity histograms show the concentration of elements within the precipitate (positive distance) and in the matrix (negative distances) shown in Figure 8. Atom maps are also shown for visualization of precipitates and atom clusters. Figure 8a shows data

for a sample of 2101-w alloy aged for 100 hours. The coarsening of the G-phase made it difficult to capture a precipitate at longer times in the small volume of the APT tip. Figure 8b-d are for alloys 2101, 2209-w and 2205, respectively, aged to 10,000 hours. No proximity histogram is shown for alloy 2003 because there were no precipitates or clustering of atoms apart from the α-α′ phase separation, which is described elsewhere [2, 21]. Atoms map for 2003 aged for 1,000 and 10,000 h are shown in Figure S6 in the Supplementary Materials.

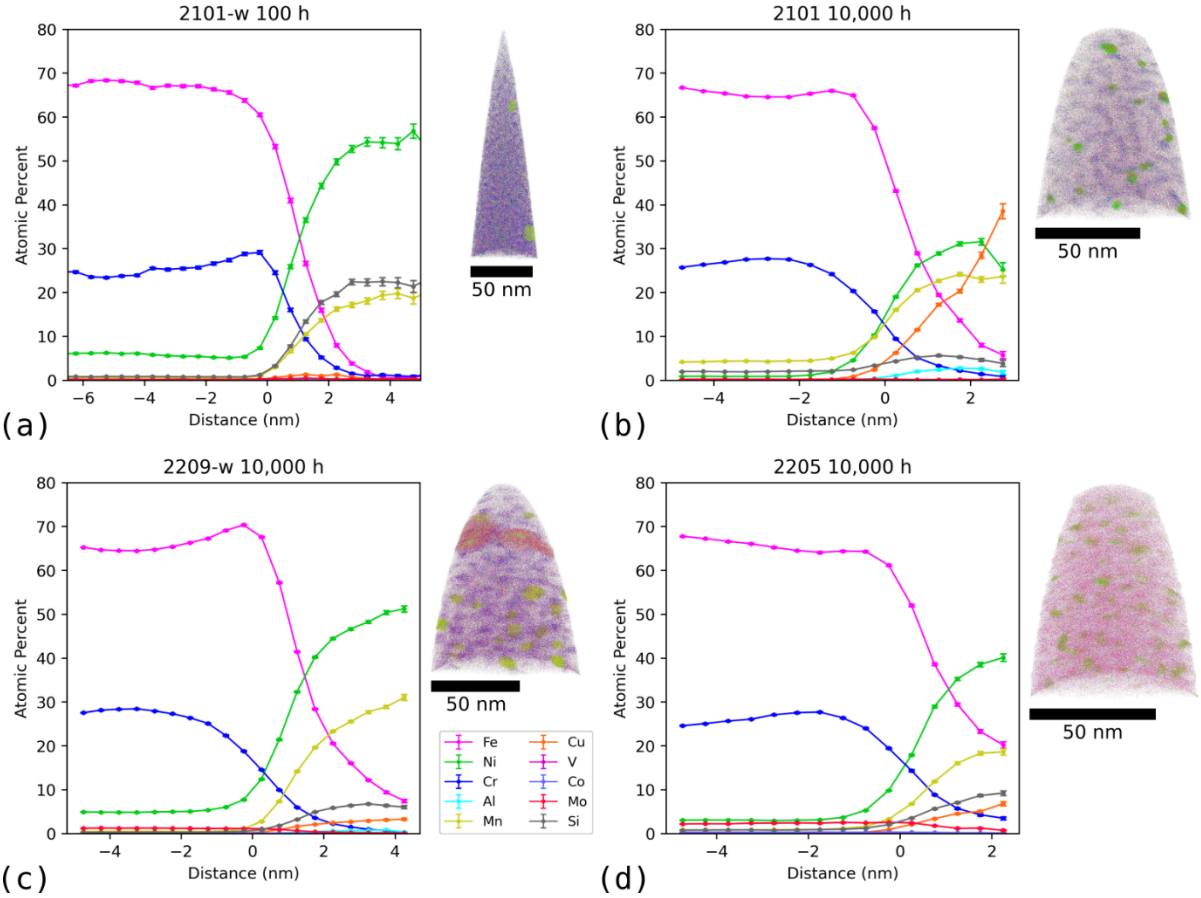

Figure 8: Proximity histograms with 15 at.% Ni isoconcentration surface and atom maps of a) 2101-w after 100h aging and b) 2101, c) 2209-w and d) 2205 after 10,000h aging at 427 °C. The histograms and atom maps have a shared color key shown in (c). The dimensions of each atom map are a) 53 nm × 177 nm, b) 74 nm × 92 nm, c) 84 nm × 106 nm, d) 61 nm × 76 nm.

The clusters in 2101-w 100 h (Figure 8a) consist primarily of Ni, Si, and Mn, in a ratio consistent with the nominal composition of the G-phase, $Ni_{16}Si_7Ti_6$, with a substitution of Mn

for Ti [26] and thus correspond to the G-phase precipitates observed in TEM images. The precipitates in 2209-w 10,000 h and 2205 10,000 h are relatively Si-poor compared to the 2101-w and the expected G-phase composition but also contain several at% of Fe which may also substitute in the G-phase [26]. The 2209-w specimen has a Mo-rich feature separate from the G-phase. It appears larger than the G-phase precipitates, but no corresponding phase was observed in either the TEM images or SAED patterns.

The Ni-containing clusters in 2101 aged for 10,000 h (Figure 8b) differs from the Ni-rich precipitates in the three other specimens, in having a lower nickel content (≈ 30 at%) and a relatively high copper content, which increases toward the center to almost 40 at%. The SAED from the 2101 10,000 h TEM specimen (Figure S7 in the Supplementary Material) has a set of faint diffraction spots separate from the ferrite phase, but do not match either the G- or other candidate precipitate phases (e.g. the ε-phase [27]). Dark field images formed with the faint diffraction spots did not show a phase distinct from the ferrite, so no further TEM analysis, such as EDS, was performed. Since the APT and TEM were performed on two separate specimens and both experimental techniques characterize only small volumes, it is uncertain if the copper-rich clusters observed in the APT correspond to the phase giving rise to the unidentified spots in Figure S7. Clusters rich in copper and nickel in 2101 aged for 200 h at 475°C have been observed by TEM EDS and bright field imaging by Silva *et al*. [11]. They called these clusters G-phase precursors, because no phase crystallographically distinct from ferrite was detected by electron diffraction. Maetz *et al.* reported the development of Ni-Mn-Si-Al-Cu rich clusters in 2101 aged 3,050 h at 420°C by APT characterization, while their TEM SAED showed no evidence of the G-phase.

The plot of G-phase volume fraction of the 10,000 h samples against equivalent nickel composition, shown in Figure 9, suggests a positive correlation between the G-phase volume fraction and total nickel equivalent composition. This is consistent with the expectation that lean grade alloys form the G-phase less readily than those with higher nickel equivalent content. The 2101 and 2003 are the two alloys that did not form a crystallographically distinct G-phase within 10,000 h at 427°C; they both have the lowest nickel content of the five alloys compared (Table 1) and the lowest equivalent (Figure 9).

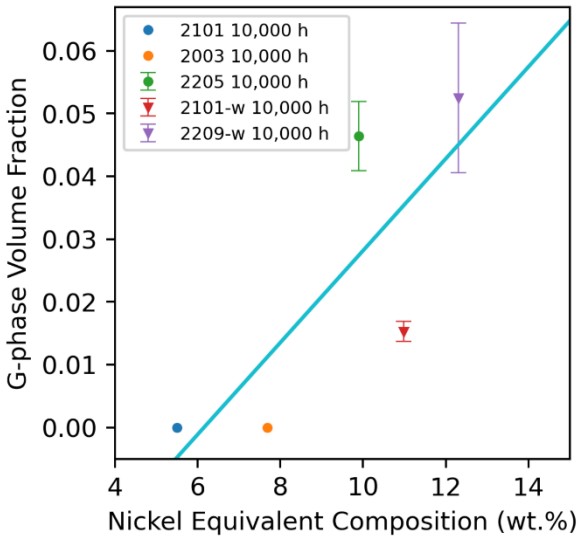

Figure 9: A plot of G-phase volume fraction against the sum of nickel equivalent elements (Ni_{eq} = Ni + 35 C + 20 N + 0.25 Cu in wt. %) [14] in the composition of each alloy. See Table 1. $R^2 = 0.62$.

4. CONCLUSIONS

The G-phase was investigated in five alloys, 2101, 2003, 2205, 2101-w, and 2209-w, at two different aging times 1,000 h and 10,000 h. The welded alloys, 2101-w and 2209-w, had observable G-phase precipitates starting at 1,000 h. Of the wrought alloys, only 2205 had observable G-phase precipitates after 10,000 h. Alloy 2101 showed evidence of a secondary phase in the diffraction pattern after 10,000 h, while 2003 did not. Lean grade alloys 2101 and 2003 are both low in Ni content, making it less thermodynamically feasible to form G-phase.

Alloy 2101 does have a higher Mn and Cu content than the other alloys, which has led to the precipitation of a different secondary phase. The weld made with alloy 2101-w has a concentration similar to that of the standard grade 2205 and 2209-w. All of these alloys formed G-phase precipitates. This study further supports the hypothesis that lean grade alloys have improved thermal stability over standard grade alloys and are better suited for long-term, elevated temperature applications. Of the five alloys studied, alloy 2003 formed no G-phase or other secondary precipitates and showed the least amount of hardening and α-α′ phase separation [2, 21]. This alloy shows the most promise for elevated temperature applications but the development of a matching lean grade weld wire is needed for practical implementation.

DATA AVAILABILITY

The experimental procedures required to reproduce these findings are available in the "Experimental methods" section. The raw data, in the form of TEM bright-field images, TEM dark-field images, diffraction patterns, and EFTEM maps, required to reproduce these microstructural findings are available to download from https://doi.org/10.7267/jh344190h/.[1]

ACKNOWLEDGEMENTS

This research was supported by the U.S. Department of Energy, Nuclear Energy University Programs under the grant DE-NE0008668. TEM was performed at the Oregon State University Electron Microscope Facility which is supported by NSF MRI Grant No. 1040588, the Murdock Charitable Trust, and the Oregon Nanoscience and Micro-Technologies Institute. The authors gratefully acknowledge the technical assistance provided by the staff of the EMF (Dr.

[1] The data has been deposited in Oregon State University's ScholarsArchive@OSU with this permanent link. The data is currently being reviewed by the OSU Library Data Management Specialist and will be available after it is approved. In the meantime, the data has been made available for review at https://oregonstateuniversity-my.sharepoint.com/:f:/g/personal/mcgiesoi_oregonstate_edu/EpPwqrID-jtDrUftp3WF070B9i7XsDk-ePVlHC46Y4PxTw?e=bi6QGW

P. Eschbach). APT research was supported by the Center for Nanophase Materials Sciences (CNMS), which is a US Department of Energy, Office of Science User Facility at Oak Ridge National Laboratory. This manuscript has been authored by UT-Battelle, LLC under Contract No. DE-AC05-00OR22725 with the U.S. Department of Energy. The United States Government retains and the publisher, by accepting the article for publication, acknowledges that the United States Government retains a non-exclusive, paid-up, irrevocable, world-wide license to publish or reproduce the published form of this manuscript, or allow others to do so, for United States Government purposes. The Department of Energy will provide public access to these results of federally sponsored research in accordance with the DOE Public Access Plan (http://energy.gov/downloads/doe-public-access-plan).

References

[1] J. Charles, Duplex stainless steels, a review after DSS'07 in Grado, Rev. Met. Paris 105(3) (2008) 155-171.

[2] J.D. Tucker, M.K. Miller, G.A. Young, Assessment of thermal embrittlement in duplex stainless steels 2003 and 2205 for nuclear power applications, Acta Materialia 87 (2015) 15-24.

[3] D.A. Garfinkel, J.D. Poplawsky, W. Guo, G.A. Young, J.D. Tucker, Phase Separation in Lean-Grade Duplex Stainless Steel 2101, JOM 67 (2015) 2216–2222.

[4] D.A. Garfinkel, Role of Alloying on the Thermal Stability of Duplex Stainless Steel, Materials Science, Oregon State University, Corvallis, OR, 2016.

[5] J.Y. Maetz, S. Cazottes, C. Verdu, F. Danoix, X. Kleber, Microstructural Evolution in 2101 Lean Duplex Stainless Steel During Low- and Intermediate-Temperature Aging, Microscopy and Microanalysis 22(2) (2016) 463-473.

[6] J.M. Vitek, G-Phase Formation In Aged Type-308 Stainless-Steel, Metallurgical Transactions A-Physical Metallurgy and Materials Science 18(1) (1987) 154-156.

[7] H.M. Chung, T.R. Leax, Embrittlement of laboratory and reactor aged CF3,CF8, and CF8M duplex stainless steels, Materials Science and Technology 6(3) (1990) 249-262.

[8] F. Danoix, P. Auger, Atom probe studies of the Fe-Cr system and stainless steels aged at intermediate temperature: A review, Materials Characterization 44(1-2) (2000) 177-201.

[9] S.L. Li, H.L. Zhang, Y.L. Wang, S.X. Li, K. Zheng, F. Xue, X.T. Wang, Annealing induced recovery of long-term thermal aging embrittlement in a duplex stainless steel, Materials Science and Engineering: A 564 (2013) 85-91.

[10] R. Badyka, G. Monnet, S. Saillet, C. Domain, C. Pareige, Quantification of hardening contribution of G-Phase precipitation and spinodal decomposition in aged duplex stainless steel: APT analysis and micro-hardness measurements, J. Nucl. Mater. 514 (2019) 266-275.

[11] R. Silva, G.S. Vacchi, C.L. Kugelmeier, I.G.R. Santos, A.A.M. Filho, D.C.C. Magalhães, C.R.M. Afonso, V.L. Sordi, C.A.D. Rovere, New insights into the hardening and pitting corrosion mechanisms of thermally aged duplex stainless steel at 475 °C: A comparative study between 2205 and 2101 steels, Journal of Materials Science & Technology 98 (2022) 123-135.

[12] X.B. Liu, C.H. Liu, J.C. Wu, X.F. Zhang, X.R. Zhu, J. Wang, Morphological instability of the G-phase induced a different contribution to hardening of ferrite phase in a duplex stainless steel, Materials Science and Engineering A-Structural Materials Properties Microstructure and Processing 832 (2022).

[13] Y.F. Chen, B. Yang, Y.T. Zhou, Y. Wu, H.H. Zhu, Evaluation of pitting corrosion in duplex stainless steel Fe20Cr9Ni for nuclear power application, Acta Materialia 197 (2020) 172-183.

[14] R.N. Gunn, Duplex Stainless Steels, Microstructure, Properties and Applications, Woodhead Publishing, 1997.

[15] T. Hamaoka, A. Nomoto, K. Nishida, K. Dohi, N. Soneda, Effects of aging temperature on G-phase precipitation and ferrite-phase decomposition in duplex stainless steel, Philosophical Magazine 92(34) (2012) 4354-4375.

[16] T. Hamaoka, A. Nomoto, K. Nishida, K. Dohi, N. Soneda, Accurate determination of the number density of G-phase precipitates in thermally aged duplex stainless steel, Philosophical Magazine 92(22) (2012) 2716-2732.

[17] S.L. Li, Y.L. Wang, X.T. Wang, F. Xue, G-phase precipitation in duplex stainless steels after long-term thermal aging: A high-resolution transmission electron microscopy study, J. Nucl. Mater. 452(1-3) (2014) 382-388.

[18] Y. Matsukawa, T. Takeuchi, Y. Kakubo, T. Suzudo, H. Watanabe, H. Abe, T. Toyama, Y. Nagai, The two-step nucleation of G-phase in ferrite, Acta Materialia 116 (2016) 104-113.

[19] Y.F. Chen, X. Dai, X.D. Chen, B. Yang, The characterization of G-phase in Fe20Cr9Ni cast duplex stainless steel, Materials Characterization 149 (2019) 74-81.

[20] W. Guo, D.A. Garfinkel, J.D. Tucker, D. Haley, G.A. Young, J.D. Poplawsky, An atom probe perspective on phase separation and precipitation in duplex stainless steels, Nanotechnology 27(25) (2016).

[21] D.A. Garfinkel, J.D. Poplawsky, W. Guo, G.A. Young, J.D. Tucker, Influence of Alloying on α-α′ Phase Separation in Duplex Stainless Steels, in: J.H. Jackson, D. Paraventi, M. Wright (Eds.) Proceedings of the 18th International Conference on Environmental Degradation of Materials in Nuclear Power Systems – Water Reactors, Springer International Publishing, Cham, 2019, pp. 2399-2408.

[22] P. Murkute, K. Oware Sarfo, I. McGieson, M.K. Santala, Y. Zhang, L. Árnadóttir, J.D. Tucker, O.B. Isgor, Effect of thermal aging on corrosion behavior of duplex stainless steels, SN Applied Sciences 4(4) (2022) 97.

[23] K. Iakoubovskii, K. Mitsuishi, Y. Nakayama, K. Furuya, Mean free path of inelastic electron scattering in elemental solids and oxides using transmission electron microscopy: Atomic number dependent oscillatory behavior, Phys. Rev. B 77(10) (2008).

[24] L. Grady, Random walks for image segmentation, IEEE Transactions on Pattern Analysis and Machine Intelligence 28(11) (2006) 1768-1783.

[25] M.K. Miller, J. Bentley, APFIM And AEM Investigation Of CF8 And CF8M Primary Coolant Pipe Steels, Materials Science and Technology 6(3) (1990) 285-292.

[26] K.H. Lo, C.H. Shek, J.K.L. Lai, Recent developments in stainless steels, Mater. Sci. Eng. R-Rep. 65(4-6) (2009) 39-104.

[27] S.W. Thompson, G. Krauss, Copper precipitation during continuous cooling and isothermal aging of a710-type steels, Metallurgical and Materials Transactions A 27(6) (1996) 1573-1588.